Transmission-Reflection-Integrated Multifunctional Continuously Tunable Metasurfaces for Decoupled Modulation of Acoustic Waves

Yugan Tang,[1] Ya Zhang,[1] Boyang Xie,[1,*] Hua Cheng,[1,†] Jianguo Tian,[1] and Shuqi Chen[1,2,3,‡]

[1] *The Key Laboratory of Weak Light Nonlinear Photonics, Ministry of Education, Renewable Energy Conversion and Storage Center, School of Physics and TEDA Institute of Applied Physics, Nankai University, Tianjin 300071, China*

[2] *The Collaborative Innovation Center of Extreme Optics, Shanxi University, Taiyuan, Shanxi 030006, China*

[3] *Collaborative Innovation Center of Light Manipulations and Applications, Shandong Normal University, Jinan 250358, China*

(Received 3 November 2021; revised 12 February 2022; accepted 25 March 2022; published 14 April 2022)

The effective modulation of acoustic fields is the most important property of acoustic metasurfaces. The realization of full-space wavefront control can significantly enhance the functionality of metasurfaces; however, the existing solutions to this problem are limited by the coupled modulations of the transmitted and reflected wavefronts. In this study, we demonstrate the possibility of controlling transmitted and reflected acoustic wavefronts in a decoupled manner with a passive structure. Simulated analyses of the parameter dependences of the transmission and reflection phases reveal that these phases can be combined arbitrarily within a range of structural parameters. Meanwhile, tunable designs increase the flexibility and simplicity of the modulation of acoustic waves. Using such a tunable structure, a transmission-reflection-integrated (TRI) metasurface is designed. By applying a single TRI metasurface, multiple independent functions are simultaneously realized in the transmitted and reflected regions, which is further confirmed by pancratic multifocal focusing (performed both experimentally and theoretically) and holographic imaging simulations. The simulated, calculated, and experimental data obtained demonstrate efficient wavefront control and excellent functional-integration performance of the TRI metasurface. In this paper, we propose a decoupled method for the simultaneous manipulation of reflected and transmitted acoustic waves, which can enhance the spatial utilization and functionality of acoustic devices.

DOI: 10.1103/PhysRevApplied.17.044027

I. INTRODUCTION

Simple and efficient modulation of acoustic waves is a basic problem in acoustics. The emergence of metamaterials with unique acoustic characteristics has considerably increased the efficiency with which acoustic waves can be modulated with simple structures, which have a wide range of applications in the field of acoustic wave manipulation, such as negative refraction, near-zero refractive index, and negative mass density [1–5]. In recent years, metasurfaces with subwavelength thicknesses have attracted considerable attention from researchers worldwide. Two-dimensional (2D) metamaterials possess simple structures, small sizes, and the ability to control wavefronts, which can be used to construct compact acoustic devices and reduce energy losses of acoustic waves. Based on the generalized Snell's law [6], many intriguing processes have been implemented by modulating the phase gradients of metasurfaces, such as wave focusing [7–11], self-bending of sound waves [12], and abnormal refraction and reflection [11,13–18]. By simultaneously manipulating either the phase and amplitude or only the phase of unit cells to form an array, acoustic holograms have been successfully produced [19–23]. Meanwhile, different images can be obtained at various distances or frequencies using only a single metasurface, which represents a simpler and more flexible technique than conventional acoustic holographic methods.

With the rapid development of metasurfaces, more attention has been paid to the realization of wave control in the full space. Traditional metasurfaces operate in either a transmitted or a reflected region; in other words, they may control wavefronts on only one side and ignore the other side. Meanwhile, the transmitted and reflected acoustic waves have not been decoupled in previous work [7–23]. From a practical viewpoint, if the transmitted and reflected wavefronts are independently decoupled and modulated, the space-utilization efficiency and functional integration of metasurfaces may be considerably enhanced. Several studies of the simultaneous manipulation of transmitted

*Corresponding author. byxie@nankai.edu.cn
†Corresponding author. hcheng@nankai.edu.cn
‡Corresponding author. schen@nankai.edu.cn

and reflected wavefronts of electromagnetic waves have been performed [24,25], but this is still a challenge for acoustic waves.

Traditional metasurfaces are composed of units with various fixed phase or amplitude responses, which require reconstruction with any change in function, resulting in a fixed frequency and a single function. This undoubtedly increases the complexity of the space and the system, as well as its inflexibility. To solve this problem and enhance the working band, researchers are increasingly focusing on tunable metamaterials and have realized many functional expansions, such as tuning with standing waves [26] or infrared radiation [27], and frequency broadening by controlling electromagnets in all active units [28]. For ultrathin metasurfaces with simple shapes, a tunable design represents a good approach to generating arbitrary radiation patterns, using a single metasurface with flexible structural unit cells. Recently, continuous control of the acoustic phase, the amplitude, or both have been implemented by adjusting the effective mass through a robust fluidic system [29], by varying the rotational angle of an inner split cavity [30], and by adjusting the length of a spiral channel [31,32]. However, such tunable metasurfaces can modulate only in either the transmitted or the reflected region, and some tuning methods are complex. Thus, a simple and tunable design with decoupled simultaneous modulation of the transmitted and reflected regions is required for broadening the application range of acoustic metasurfaces.

Herein, we propose a transmission-reflection-integrated (TRI) multifunctional continuously tunable acoustic metasurface and realize decoupled control of both the transmitted and the reflected wavefronts of acoustic waves. The structural units of such metasurfaces are based on coated unit cells and perforated panels [21]. By tuning specific structural parameters, the unit cell can be made to continuously and independently manipulate different phases of the transmitted and reflected acoustic waves with high flexibility and simplicity. In addition, acoustic focusing and holographic imaging studies are performed to validate the performance of the TRI metasurface.

II. INVERSE DESIGN STRATEGY

Figure 1 shows a conceptual illustration of a TRI multifunctional continuously tunable acoustic metasurface, which can independently control both the transmitted and the reflected waves under irradiation with a plane acoustic wave. The structural units that the TRI metasurface is composed of are depicted in the top right of Fig. 1. The structures inside the yellow dashed boxes are tunable to manipulate the reflection and transmission phase responses. The unit cell represents a multilayer structure evolved from a labyrinthine structure [Fig. 2(a)], which is composed of parts related to transmission and reflection. The upper part consists of a labyrinthine structure and two

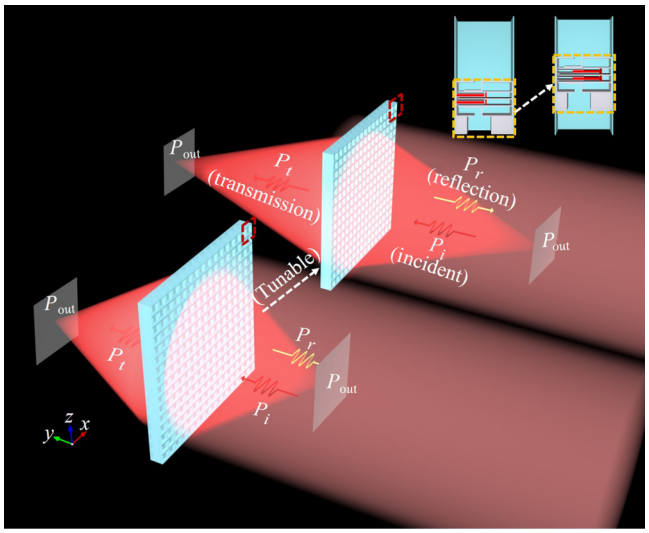

FIG. 1. Conceptual illustration of a tunable TRI metasurface. A single metasurface can be used to simultaneously realize multiple functions in the transmitted and reflected regions. By tuning the unit cell structure, the functional performance of the metasurface can be changed.

rectangular cavities symmetrically placed at the top and bottom. For each unit cell, the bottom cavity serves as the entrance, while the top cavity serves as the exit, to stabilize the resonant frequency of the structure. In the middle of the two cavities, four plates with thickness d_i form two rectangular channels with a height w_i and length $0.24\lambda_0$ ($\lambda_0 = 10$ cm) in the horizontal direction, which can be used to move the red matching plates. Thus, the channel length l_t can be adjusted to realize phase modulation of the transmitted waves. The red matching plates are composed of vertical and horizontal plates. By fixing the position of the blue plate and moving the middle two parts in the vertical direction, the length of the reflection channel h_r can be varied to modulate the phase of the reflected waves. To investigate the reflection and transmission properties of the unit cells, full-wave simulations are performed to simulate their amplitudes and phases using the commercial software package COMSOL Multiphysics. The thermoviscous acoustic module is employed to consider both friction and thermal diffusivity in the metasurface region. The pressure module is used in the incident and transmitted regions [33]. The working frequency is set to 3450 Hz. The structural walls are assumed to be acoustically rigid, and the immersion medium is air, with a speed of sound $c_0 = 345$ m/s and mass density $\rho_0 = 1.2$ kg/m^3.

Realization of decoupled modulation of the reflection and transmission phases means that the reflection phase ϕ_r is not affected when the transmission phase ϕ_t is modulated, and vice versa. An intuitive way to conduct decoupled modulation is to manipulate ϕ_t and ϕ_r separately using a single parameter. By employing the relationship between

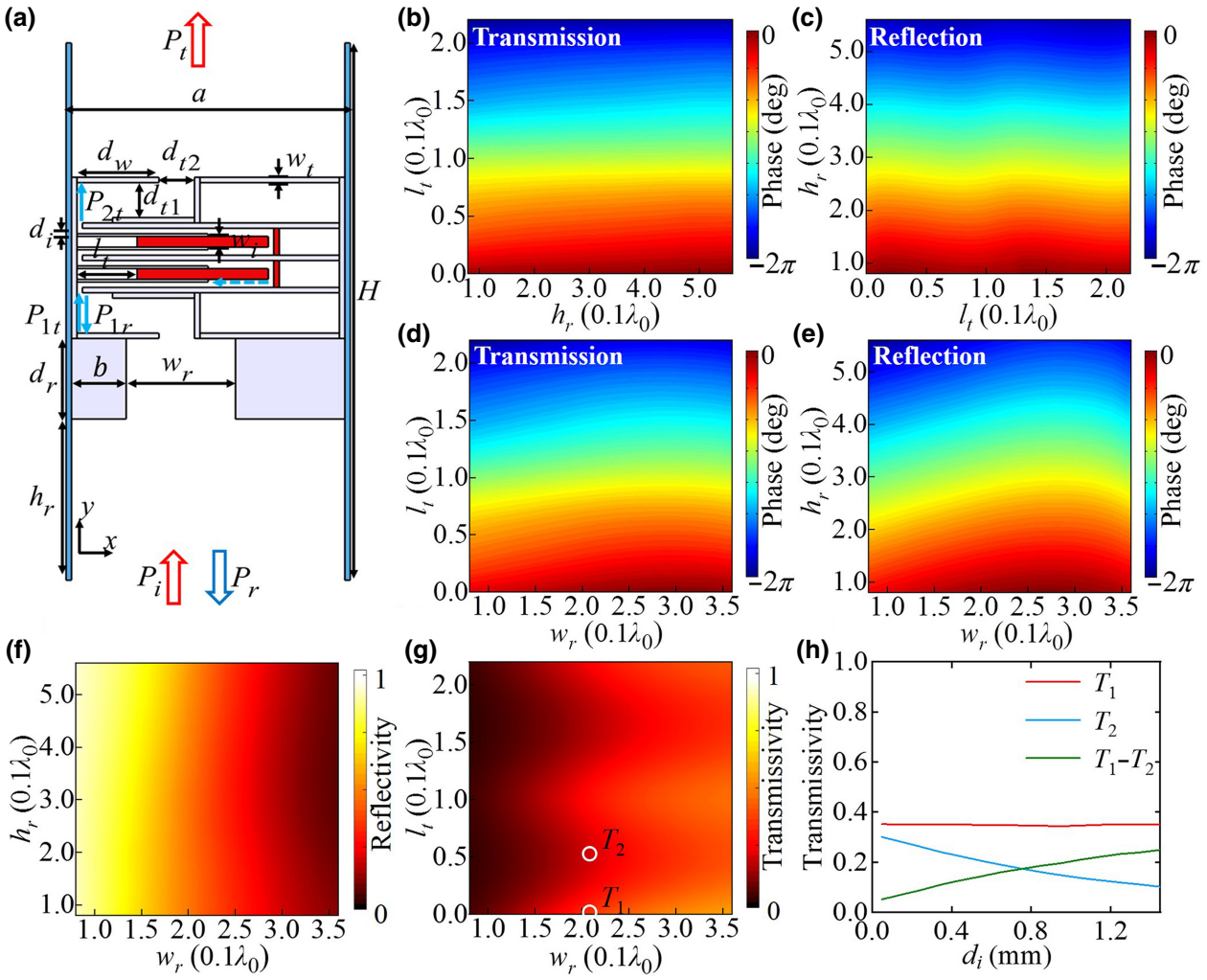

FIG. 2. Unit geometry and its simulated acoustic responses. (a) 2D cross section of the structural unit cell. The red matching plates, the blue plates, and the perforated panel, with width w_r, are utilized to modulate the transmission phase, reflection phase, and transmissivity or reflectivity, respectively. The parameters from top to bottom are $a = 0.52\lambda_0$, $d_w = 0.15\lambda_0$, $d_{t2} = 0.0715\lambda_0$, $w_t = 0.01\lambda_0$, $d_{t1} = 0.065\lambda_0$, $d_i = 0.005\lambda_0$, $w_i = 0.02\lambda_0$, $d_r = 0.15\lambda_0$, $b = 0.1\lambda_0$, $w_r = 0.21\lambda_0$, and $H = \lambda_0$. (b),(c) Variations in the (b) transmission and (c) reflection phases with structural parameters l_t and h_r. (d) Variations in the transmission phase with structural parameters l_t and w_r. (e) Variations in the reflection phase with structural parameters h_r and w_r. (f) Relationship between the reflectivity and structural parameters h_r and w_r with a fixed parameter $l_t = 0.1\lambda_0$. (g) Relationship between the transmissivity and structural parameters l_t and w_r with a fixed parameter $h_r = 0.3\lambda_0$. (h) Variations of the high transmissivity (T_1), low transmissivity (T_2), and fluctuation range ($T_1 - T_2$) with d_i.

the wave path and the phase and fixing the phase of the incident wave, ϕ_t and ϕ_r can be analytically expressed as

$$\phi_t = -\frac{8\pi l_t}{\lambda_0} + \phi_{t0}, \tag{1}$$

$$\phi_r = -\frac{4\pi h_r}{\lambda_0} + \phi_{r0}, \tag{2}$$

where the constants ϕ_{t0} and ϕ_{r0} are the initial transmission and reflection phases, respectively.

Meanwhile, for the simultaneous modulation of acoustic waves in both the transmitted and the reflected regions, with structural parameters l_t and h_r, the transmitted and reflected energies need to be investigated to ensure high modulation efficiency. The widths of the left and right blue plates are w_t. The width of the lower channel is $(a - 2w_t) = \beta a$. The filling ratio of the designed structural unit cells is $\beta \approx 1$, which implies that the reflectivity is not affected by h_r [22]. Compared with an ordinary labyrinthine structure, four grooves with length $l_r = l_t + w_t$ and thickness $d = d_i + w_t$ are formed between three plates and the two horizontal red plates in the tunable design, as indicated by the dashed blue arrow in Fig. 2(a). Thus, mutated interfacial conditions are formed between

channels with thicknesses w_t and d. The channels at the bottom and the top of the labyrinthine structure are the entrance and exit, respectively, indicated by the solid blue arrows in Fig. 2(a). The transfer matrix M and boundary matrix Q_1 can be written as

$$M(x) = \begin{bmatrix} e^{ikx} & 0 \\ 0 & e^{-ikx} \end{bmatrix}, \tag{3}$$

$$Q_1 = \frac{1}{2}\begin{bmatrix} 1+Z_{12} & 1-Z_{12} \\ 1-Z_{12} & 1+Z_{12} \end{bmatrix}, \tag{4}$$

where $Z_{12} = Z_1/Z_2 = d/w_t$, and Z_1 and Z_2 are the acoustic impedances of channels with widths w_t and d, respectively. The relationship between the sound waves at the entrance (P_{1t} and P_{1r}) and the exit (P_{2t}) can be simplified to

$$\begin{bmatrix} P_{1t} \\ P_{1r} \end{bmatrix} \approx Q_1' M(4l_r) Q_1'^{-1} \begin{bmatrix} P_{2t} \\ 0 \end{bmatrix}, \tag{5}$$

where $Q_1' = \left[\begin{smallmatrix} 1 & 0 \\ 0 & -1 \end{smallmatrix}\right] Q_1$. Considering the influence of the reflective layer, with a thickness of d_r, the total transmissivity and reflectivity can be expressed as

$$T_{\text{tot}} = \alpha T_{\text{lab}} T_{\text{ref}}, \tag{6}$$

$$R_{\text{tot}} = 1 - T_{\text{lab}} T_{\text{ref}}, \tag{7}$$

where α is the loss factor, $T_{\text{lab}} = 1/\left[\cos^2 4kl_r + (d/2w_t + w_t/2d)^2 \sin^2 4kl_r\right]$, and $T_{\text{ref}} = 1/\left[\cos^2 kd_r + (a/2w_r + w_r/2a)^2 \sin^2 kd_r\right]$. If there are channels with mutated cross sections in the labyrinthine structure ($d/w_t \neq 1$), different channel lengths will cause different transmissivities. For fixed d_r and w_r, when $4kl_r = (2n-1)\pi/2$ ($n = 1, 2, \ldots$), the transmissivity is minimum. When $4kl_r = n\pi$ ($n = 0, 1, \ldots$), the transmissivity is maximum. When w_r increases in the range from 0 to a, the transmissivity and reflectivity increase and decrease, respectively, for a fixed d_r, indicating that w_r can be simultaneously utilized to control the transmissivity and reflectivity properties.

To study the modulation of the transmission and reflection phases by the structural parameters, we simulate the variations of the transmission and reflection phases for different structural parameters l_t and h_r, as shown in Figs. 2(b) and 2(c), respectively. We also give the variation of the transmission phase with the structural parameters l_t and w_r and that of the reflection phase with the structural parameters h_r and w_r in Figs. 2(d) and 2(e), respectively. The results show that decoupled modulation of the transmission and reflection phases from 0 to 2π can be easily realized for different structural parameters. The variation of the reflectivity with the structural parameters h_r and w_r and that of the transmissivity with the structural parameters l_t and w_r are given in Figs. 2(f) and 2(g), respectively. The loss factor of most unit cells is about 60%. The two white circles represent the high transmissivity T_1 and low transmissivity T_2. The modulations of the phases and energies are nearly decoupled. Thus, the phases or the transmissivity (or reflectivity) can be individually controlled by one parameter. Figure 2(h) displays the simulated variations of T_1, T_2, and the fluctuation range $(T_1 - T_2)$ for different d_i. T_1 can maintain a relatively large value, while T_2 and $T_1 - T_2$ increase and decrease, respectively, with a decrease in d_i. To maintain a stable transmissivity, we can either change the value of w_r or reduce the magnitude of d_i. Owing to the symmetrical design used in the subsequent work, the values of the transmissivity or reflectivity do not affect the position and full width at half maximum (FWHM) of the focal point; for this reason, the values of w_r and d_i are fixed at $0.21\lambda_0$ and $0.005\lambda_0$, respectively.

III. EXPERIMENT

The designed structure can be used to program a decoupled tunable TRI metasurface. Figure 3(a) shows a photograph of the tunable unit cells, fabricated by three-dimensional (3D) printing with a precision of 0.1 mm. These cells contain the main structures and movable matching plates depicted in Fig. 2(a). To ensure that the channel width between the horizontal and vertical matching plates is fixed at w_t, we place two connecting cylinders with diameters of 1 mm between these plates, one at the top and the other one at the bottom [see the top right corner of Fig. 3(a)]. The observed structural changes in the sample are shown in Fig. 3(b). By horizontally moving the two matching plates with thickness w_i in the labyrinthine structure, the transmission phase can be flexibly modulated, as indicated by the red arrows. The reflection phase can also be modulated by moving the middle structure in the vertical direction inside the matched groove with width a and height H, as indicated by the blue arrows.

To evaluate the performance of the metasurface, we perform experiments in an acoustic waveguide, as shown in Fig. 3(c). The size of the entire waveguide is $200 \times 150 \times 3$ cm^3. The sample is placed in the middle of the waveguide and firmly sandwiched. Acoustical absorbent materials are placed around the waveguide to form an artificial perfect matching layer (PML). A speaker array composed of circular planar speakers with diameters of 25 mm is used to form a plane-wave sound source at the right boundary, located at a sufficiently large distance from the metasurface. There are two black-colored rectangular measurement areas shown in the figure, in the transmitted and reflected regions. The acoustic fields are comprehensively scanned with one microphone (B&K 4961, 1/4-inch diameter) in the two black rectangular areas with a step size of 1 cm in the frequency range from 3000 to 4000 Hz; these fields are denoted p_t (transmitted acoustic field) and p_r (reflected acoustic field). To obtain the reflected acoustic field, we scan the reflection area twice: first without the

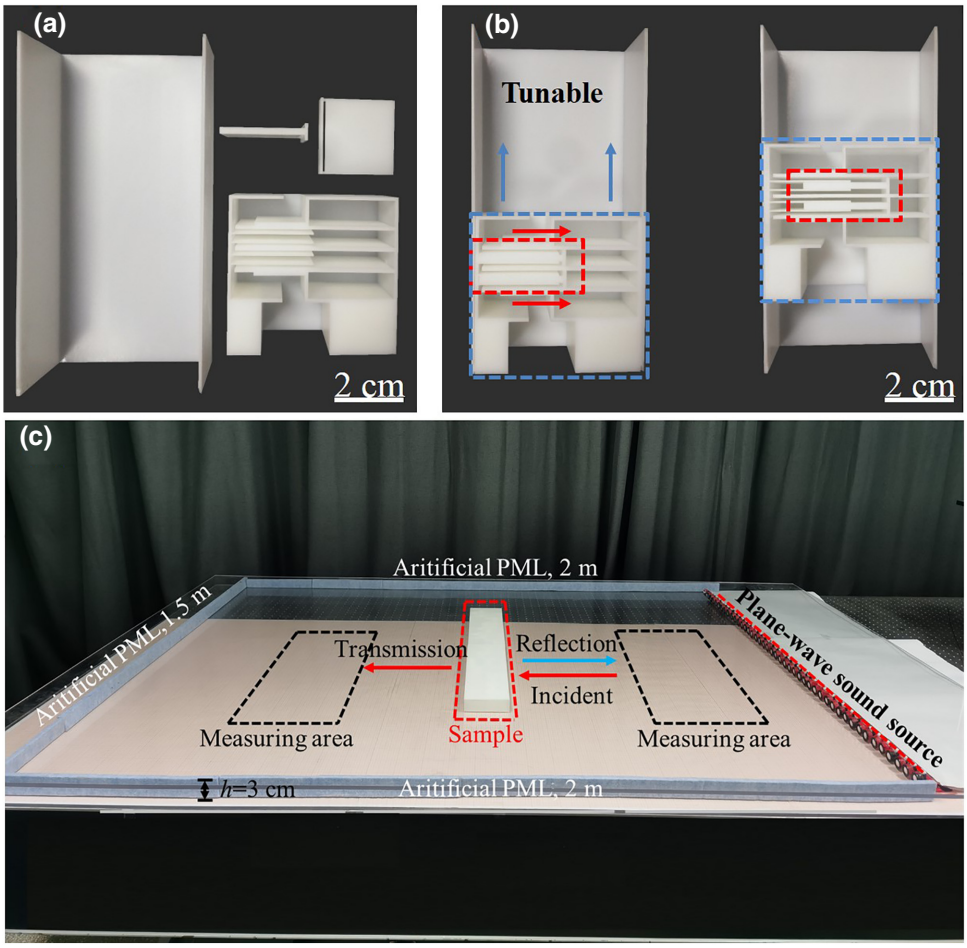

FIG. 3. (a) Photograph of the fabricated tunable structural unit cell and (b) illustration of the structural tuning process. The red and blue arrows indicate two tunable modes. (c) Photograph of the acoustic waveguide used for experimental studies, in which absorbing foam is placed around an artificial perfect matching layer (PML). The plane-wave source array is denoted by the red line, the metasurface is designated by the red rectangle, and the measurement areas are located inside the black rectangles.

sample (measured as p_i), and second with the sample (measured as p_r'). The reflected acoustic field is calculated from the formula $p_r = p_r' - p_i$, and we take the same approach to the reflected sound waves as in the simulations. To analyze the measured sound signal, we use a Keysight E5061B ENA vector network analyzer, which can extract the amplitude and phase of a sound wave.

IV. RESULTS AND DISCUSSION

To examine the effect of the tunable unit cells, we design a TRI metasurface functioning as a pancratic acoustic lens. First, we introduce a single-focus pancratic TRI acoustic lens, schematically depicted in Fig. 4(a). The metasurface consists of a one-dimensional array of 16 TRI unit cells (total length $16 \times a = 83.2$ cm), generating two focal points in the transmitted and reflected regions under plane-wave irradiation. The focal length can be easily adjusted by means of the tunable structure, as indicated by the red hollow arrow in Fig. 4(a). To obtain a metasurface sequence, we adopt the interference principle to evaluate the phase distributions of the lens. In addition, the same phase is chosen at symmetric positions on both sides of the central axis to simplify the lens design. Generally, sound waves produce constructive interference at the focal point. Thus, for the two symmetric ith unit cells located at $(x_i, 0)$ and $(-x_i, 0)$ $(x_i > 0)$, the phase ϕ_i' at the focal point should satisfy the following relationship:

$$-k\left(\sqrt{x_i^2 + f^2} - f\right) + \phi_i - \phi_0 = 2n\pi, \qquad (8)$$

where ϕ_i is the phase of the ith unit cell, n is an integer, and f is the focal length. When the phase of the central unit ϕ_0 is specified, discrete phase distributions can be calculated for the lens in both the transmitted and the reflected regions. A structural sequence is obtained by integrating the unit cells into a tunable TRI metasurface.

To demonstrate its pancratic capability, we calculate two metasurface sequences, containing two different focal lengths in the transmitted and reflected regions. For this purpose, we set the focal lengths to $f_1 = 40$ cm and $f_2 = 60$ cm and the working frequency to 3450 Hz. Four or six unit cells are present in the central region, with $\phi_0 = -2\pi$ $(l_t = 0, h_r = 0.08\lambda_0)$ for both the transmission and the reflection phases. Based on Eq. (8), the phases of the other unit cells can be calculated. Thus, the specific parameters l_t and h_r of each unit cell required to tune the structure

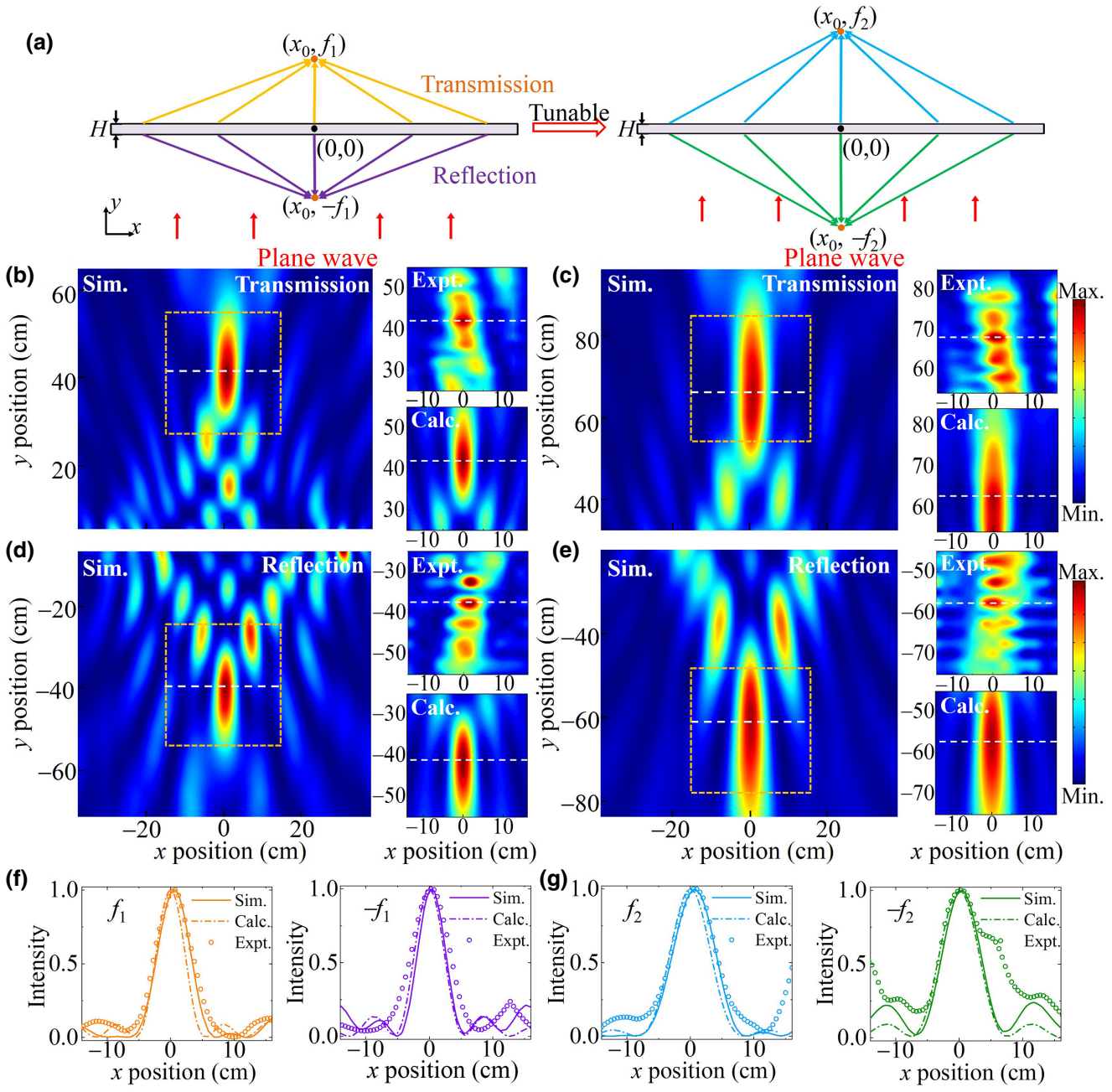

FIG. 4. (a) Schematic illustration of TRI pancratic acoustic lens with focal lengths $f_1 = 40$ cm and $f_2 = 60$ cm. (b)–(e) Simulated (on the left sides), experimental (in the top right corners), and calculated (in the bottom right corners) pressure intensity field distributions of the TRI lens in the (b),(c) transmitted and (d),(e) reflected regions, with focal lengths f_1 and f_2, respectively. The yellow dashed boxes indicate the measured and calculated regions. (f),(g) Simulated (lines), measured (circles), and calculated (dotted lines) normalized intensity curves in the focal plane, extracted from the horizontal white dashed lines in the corresponding diagrams for $f_1 = 40$ cm and $f_2 = 60$ cm, respectively. The left and right graphs in each part are the transmitted and reflected focal-plane intensity curves, respectively.

can be obtained, as shown in Table I. The selection of x_i is based on one side of the unit cell, except that the transmission for a focal length of 40 cm is based on the center of the unit cell (in order to have an accurate focus position). Based on the phase responses designed by use of Eq. (8), we also calculate the pressure intensity fields. The simulated, measured, and calculated pressure-focusing intensity fields of the transmitted and reflected regions with a focal length f_1 are plotted in the left, top right, and bottom right parts, respectively, of Figs. 4(b) and 4(d) [Figs. 4(c) and 4(e) show corresponding results for f_2]. The measured and calculated pressure intensity fields correspond to the

TABLE I. Parameters of each unit cell, obtained for focal lengths of 40 and 60 cm.

	Parameter	$i=1$	$i=2$	$i=3$	$i=4$	$i=5$	$i=6$	$i=7$	$i=8$
$f_1=40$ cm	$l_t(\lambda_0)$	0	0	0.2	0	0.09	0.02	0.19	0.11
	$h_r(\lambda_0)$	0.08	0.08	0.51	0.43	0.33	0.19	0.54	0.38
	$w_r(\lambda_0)$	0.21	0.21	0.21	0	0.21	0.21	0.21	0.21
$f_2=60$ cm	$l_t(\lambda_0)$	0	0	0	0.2	0	0.12	0.06	0
	$h_r(\lambda_0)$	0.08	0.08	0.08	0.48	0.4	0.31	0.2	0.09
	$w_r(\lambda_0)$	0.21	0.21	0.21	0.21	0	0.21	0.21	0.21

yellow dashed boxes for the simulated results. It can be seen that focusing phenomena emerge simultaneously in the two regions when the sound wave illuminates the metasurface perpendicularly. A comparison of the measured, simulated, and calculated sound intensity field distributions shows that the focus positions for transmission and reflection are accurate, except for a slight discrepancy, and both can exhibit excellent focusing performance for a 1×16 lens. The simulated, measured, and calculated focal lengths for f_1 are 42 cm, 42 cm, and 42 cm, respectively, for transmission and -40 cm, -38 cm, and -41 cm for reflection (66 cm, 68 cm, and 63 cm, and -61 cm, -58 cm, and -57 cm, respectively, for f_2). The simulated and measured focus positions agree well with the calculation results, which proves the accuracy of the phase responses of the unit cells. Meanwhile, for a single metasurface, by tuning the characteristic parameters of the structural unit cells, the focal points for both transmission and reflection can be changed precisely, which proves the accuracy of the tuning method for the unit cells in the experiment.

For a more quantitative comparison, the separately normalized horizontal pressure intensity fields at the focal points along the x direction (indicated by the white dashed line) are shown in Fig. 4(f) for f_1 [and in Fig. 4(g) for f_2]. The corresponding simulated, measured, and calculated FWHMs of the focal points in the x direction are found to be $0.57\lambda_0$, $0.65\lambda_0$, and $0.50\lambda_0$, respectively, in the transmitted region and $0.50\lambda_0$, $0.66\lambda_0$, and $0.51\lambda_0$ in the reflected region for f_1, and $0.77\lambda_0$, $0.78\lambda_0$, and $0.71\lambda_0$ in the transmitted region and $0.70\lambda_0$, $1.00\lambda_0$, and $0.70\lambda_0$ in the reflected region for f_2. The diffraction resolution limits at 3450 Hz are $0.59\lambda_0$ for f_1 and $0.88\lambda_0$ for f_2, in theory. Both the simulation and the calculation results show similar FWHMs of the transmitted and reflected focal points, which indicates that the phase responses of the transmission and reflection are consistent. However, since the length of the plane-wave source is greater than the length of the lens (140 cm $>$ 83.6 cm), in addition to the waves transmitted through the lens, there are diffracted waves on both sides of it. Thus, the transmitted focal lengths are slightly larger than the theoretical focal lengths, while the reflected focal lengths are not. Besides, the experimental results show that both the transmission and the reflection pressure intensity fields exhibit fluctuation patterns, especially in the reflected region. The fluctuations in the transmitted region may be attributed to fabrication error and to leakage of background waves, which can be improved by increasing the number of unit cells and reducing the leakage of waves. The fluctuations in the reflected region, which are caused by the superposition of sound waves reflected from the source interface and waves reflected from the metasurface, can be improved by increasing the distance between the source and the metasurface and by decreasing the reflection at the source in the experiments.

The difference between the theoretical diffraction limit and the FWHM of the focal points increases with an increase in the focal length. This means that the pancratic acoustic lens has great ability for imaging. In contrast to a conventional acoustic lens based on a metasurface, the TRI pancratic lens adds a reflected part on the basis of transmitted focusing to achieve more functions. The tunable structural characteristics also enable us to flexibly manipulate the focal length of the lens.

Next, we design a multifocus lens using a combination of two types of lenses. This consists of 28 unit cells (total length $28 \times a = 145.6$ cm), with two focal points in both the transmitted and the reflected regions. The 14 unit cells on the left side are used to construct a lens with a focal length $y_1 = 40$ cm, and the other 14 unit cells on the right side are used to achieve a focal length $y_2 = 60$ cm. The corresponding structural parameters, listed in Table I, can also be used to design TRI units, where i is varied from 1 to 7. The simulated, measured, and calculated pressure intensity fields of the multifocal TRI lens determined in the transmitted and reflected regions are shown in Figs. 5(a) and 5(b), respectively. A comparison between the experimental, calculated, and simulated results reveals that the multifocal lens exhibits excellent performance characteristics except for a little interference between the two focal points on the same side. We also plot the simulated, measured, and calculated horizontal pressure intensity curves (normalized separately) for the transmitted and reflected regions at the focal points in Fig. 5(c), which are in good agreement with each other. The simulated, measured, and calculated positions of the focal points determined for the lines, circles, and dotted lines are $y = 37$ cm, 39 cm, and 36 cm (yellow); 58 cm, 59 cm, and 63 cm (blue); -37 cm, -39 cm, and -37 cm (purple); and -57 cm, -57 cm, and -60 cm (green). Compared with the single-focus

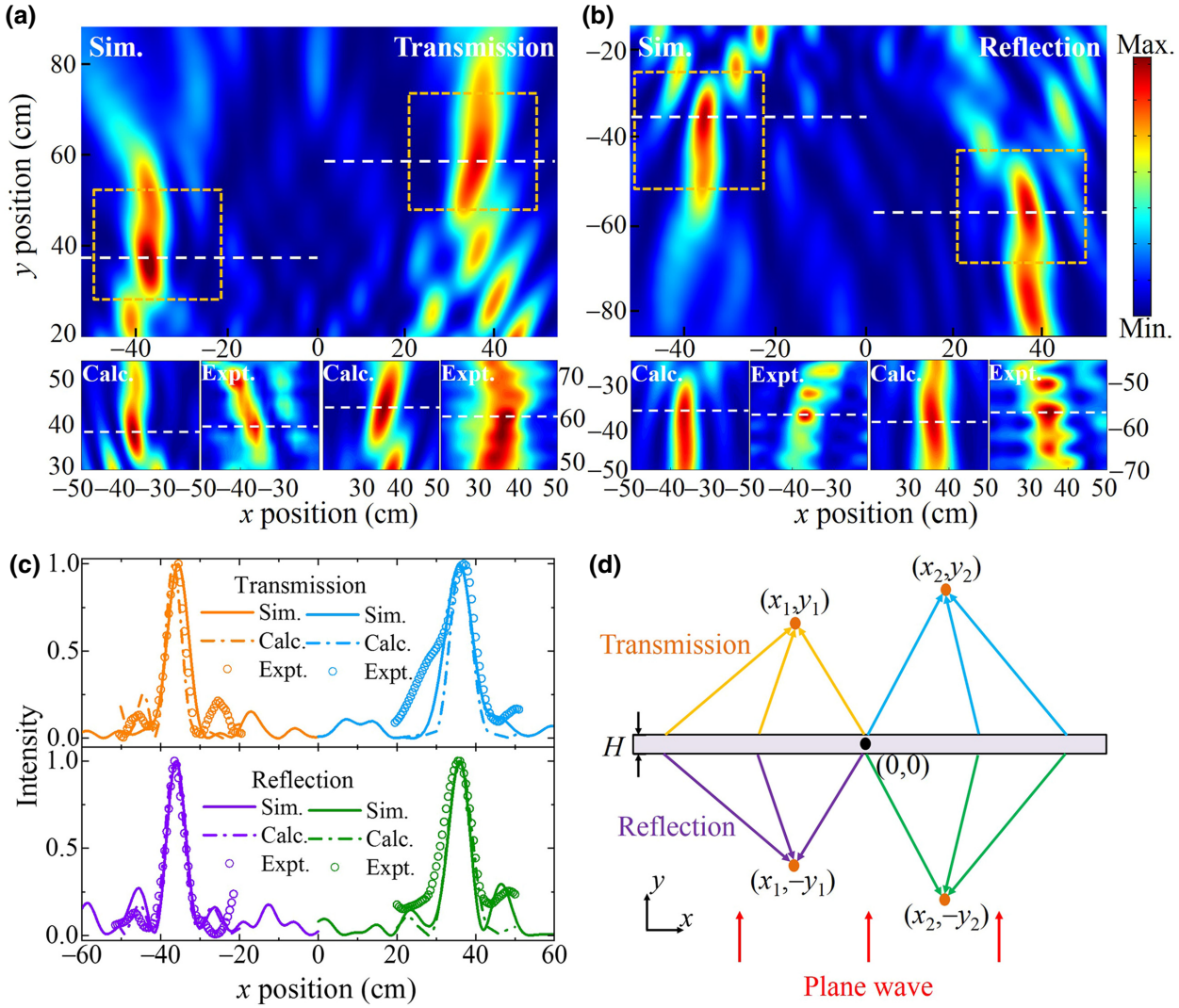

FIG. 5. (a),(b) Simulated, experimental, and calculated pressure intensity field distributions of the multifocus TRI acoustic lens in the (a) transmitted and (b) reflected regions. The yellow dashed boxes indicate the measured and calculated regions. (c) Simulated (lines), measured (circles), and calculated (dotted lines) normalized intensity curves, extracted from the horizontal white dashed lines in the corresponding diagrams. (d) Schematic illustration of the multifocus TRI acoustic lens with focal lengths $y_1 = 40$ cm and $y_2 = 60$ cm.

lens, the multifocus lens contains more unit cells, which allow a larger number of sound waves to pass, resulting in better focusing. In addition, since the length of the plane-wave source is similar to the length of the multifocus lens, the positions of the transmission focal points are consistent with the theoretical results. As expected, the measured FWHM values of the focal points of the multifocus lens are in good agreement with the simulation and calculation results. Finally, an overall schematic diagram of the multifocus acoustic lens is shown in Fig. 5(d). This demonstrates the high flexibility and the ability to realize a pancratic TRI lens, which has many prospective applications in the field of acoustics.

We further extend the proposed design to 2D cases and demonstrate that the unit cells described here can be used to obtain a TRI acoustic hologram. By applying an angular-spectrum iteration method [34,35], phase distributions on the metasurface are calculated from the acoustic pressure fields $p(x,y,z)$ of the target image. The backpropagation from the target image ($z = z_0$) to the metasurface ($z = 0$) is determined via the following formulas:

$$P\left(k_x, k_y, 0\right) = P\left(k_x, k_y, z_0\right) \exp\left(-iz_0\sqrt{k_0^2 - k_x^2 - k_y^2}\right), \tag{9}$$

$$p\left(x, y, 0\right) = \frac{1}{4\pi^2} \iint P\left(k_x, k_y, 0\right)\, dk_x\, dk_y, \tag{10}$$

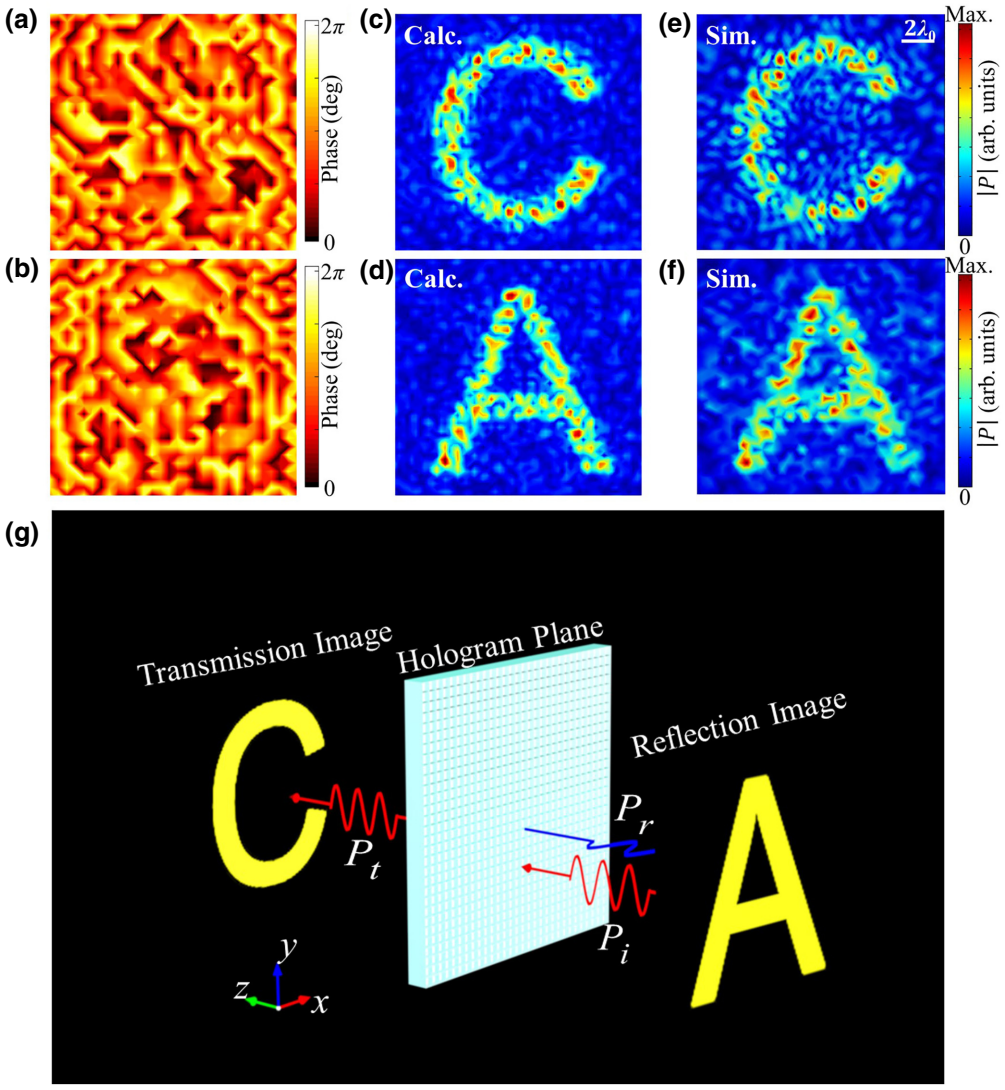

FIG. 6. (a),(b) Theoretically calculated holographic phase distributions on the metasurface for transmission (a) and reflection (b). (c),(d) Calculated pressure amplitude distributions in the imaging plane for transmission (c) and reflection (d). (e),(f) Corresponding simulation results in the imaging plane for transmission (e) and reflection (f). (g) 3D conceptual illustration of simultaneous holographic imaging performed in the transmitted and reflected regions.

where $p(x, y, 0)$ and $P(k_x, k_y, 0)$ are the acoustic pressure field and the angular spectrum, respectively, at $z = 0$. As an illustration, two square images depicting the letters "C" and "A" with a size $15.6\lambda_0$ are used as target images in the transmitted and reflected regions, respectively. Diffraction-limited performance is achieved when the size of the unit cell is equal to a half of the wavelength [19]; therefore, we set the size of the unit cell to $0.52\lambda_0 \times 0.52\lambda_0 \times \lambda_0$, and the transmissivity of all unit cells is fixed at 0.5. The imaging positions are $z_r = -4.5\lambda_0$ for reflection and $z_t = 4\lambda_0$ for transmission. In order to simplify the calculation and simulation, we discretize the phase distributions of the metasurface as ten discrete phases with a step size of $\pi/5$. The reflection and transmission phase distributions on the metasurface obtained via Eq. (9) are shown in Figs. 6(a) and 6(b), respectively. The calculated and simulated pressure amplitude distributions of the reconstructed images under plane-wave irradiation are shown in Figs. 6(c) and 6(e) for transmission and in Figs. 6(d) and 6(f) for reflection. Because of the small number of unit cells, there are some fluctuations in the amplitude distributions, which can be improved by increasing the number. When the two holographic phase distributions are integrated into a TRI metasurface, acoustic holographic images are obtained in both the transmitted and the reflected regions with the same incident acoustic plane wave [Fig. 6(g)]. Hence, TRI holograms are more functional and flexible than the previously reported acoustic holograms.

V. CONCLUSION

In this study, we design tunable structures that can serve as basic unit cells to develop TRI multifunctional metasurfaces for decoupled modulation of transmitted and reflected wavefronts. The unit cells enable flexible control in the all-phase range by varying the acoustic path difference, as confirmed by the results of numerical simulations. Several metasurfaces based on the designed structures with good wave-focusing and pancratic properties are

developed and verified, both theoretically and experimentally. In addition, the proposed TRI metasurfaces exhibit excellent holographic characteristics and provide another degree of freedom for sound-field regulation, which can potentially be applied in acoustic devices for the passive control of full-space wavefronts. With the new degree-of-freedom response, the TRI design can realize independent wavefront manipulation in transmitted and reflected regions, such as the two sides in asymmetrical wavefront manipulation and asymmetric holographic encryption. More complex functions can also be implemented based on a combination of controls of two regions, such as using one region as a control switch for the other. Meanwhile, the results are extremely useful for expanding the acoustic applications of such tunable TRI metasurfaces, which can flexibly implement switchable acoustic functions, dynamic transformation of holographic imaging, and beam steering at different angles. In the future, combined with smaller and active designs, TRI acoustic metasurfaces can be developed with capabilities for high-resolution imaging and active tunable control. Owing to the efficient utilization of space, such metasurfaces can be extended to acoustic focusing, particle manipulation, medical acoustic imaging, and wave-field-modulation applications in the full space.

ACKNOWLEDGMENTS

This work was supported by the National Key Research and Development Program of China (Grants No. 2021YFA1400601 and No. 2017YFA0303800), the National Natural Science Fund for Distinguished Young Scholars (Grant No. 11925403), the National Natural Science Foundation of China (Grants No. 12122406, No. 12192253, and No. 11974193), and the Natural Science Foundation of Tianjin for Distinguished Young Scientists (Grant No. 18JCJQJC45700).

[1] Z. Liang and J. Li, Extreme Acoustic Metamaterial by Coiling up Space, Phys. Rev. Lett. **108**, 114301 (2012).

[2] G. C. Ma and P. Sheng, Acoustic metamaterials: From local resonances to broad horizons, Sci. Adv. **2**, e1501595 (2016).

[3] Y. Li, B. Liang, Z. M. Gu, X. Y. Zou, and J. C. Cheng, Reflected wavefront manipulation based on ultrathin planar acoustic metasurfaces, Sci. Rep. **3**, 2546 (2013).

[4] Y. Cheng, C. Zhou, B. G. Yuan, D. J. Wu, Q. Wei, and X. J. Liu, Ultra-sparse metasurface for high reflection of low-frequency sound based on artificial Mie resonances, Nat. Mater. **14**, 1013 (2015).

[5] Y. Li and M. B. Assouar, Three-dimensional collimated self-accelerating beam through acoustic metascreen, Sci. Rep. **5**, 17612 (2015).

[6] N. Yu, P. Genevet, M. A. Kats, F. Aieta, J. P. Tetienne, F. Capasso, and Z. Gaburro, Light propagation with phase discontinuities: Generalized laws of reflection and refraction, Science **334**, 333 (2011).

[7] Y. Li, X. Jiang, R. Q. Li, B. Liang, X. Y. Zou, L. L. Yin, and J. C. Cheng, Experimental Realizations of Full Control of Reflected Waves with Subwavelength Acoustic Metasurfaces, Phys. Rev. Appl. **2**, 064002 (2014).

[8] F. Aieta, P. Genevet, M. A. Kats, N. Yu, R. Blanchard, Z. Gaburro, and F. Capasso, Aberration-free ultra-thin flat lenses and axicons at telecom wavelengths based on plasmonic metasurfaces, Nano Lett. **12**, 4932 (2012).

[9] K. Tang, C. Qiu, J. Lu, M. Ke, and Z. Liu, Focusing and directional beaming effects of airborne sound through a planar lens with zigzag slits, J. Appl. Phys. **117**, 024503 (2015).

[10] R. Al Jahdali and Y. Wu, High transmission acoustic focusing by impedance-matched acoustic meta-surfaces, Appl. Phys. Lett. **108**, 031902 (2016).

[11] K. Tang, C. Qiu, M. Ke, J. Lu, Y. Ye, and Z. Liu, Anomalous refraction of airborne sound through ultrathin metasurfaces, Sci. Rep. **4**, 06517 (2014).

[12] L. Zhang, Y Li, X. Jiang, B. Liang, and J. C. Cheng, Metascreen-based acoustic passive phased array with subwavelength resolution, J. Acoust. Soc. Am. **138**, 1752 (2015).

[13] Y. Xie, W. Wang, H. Chen, A. Konneker, B. I. Popa, and S. A. Cummer, Wavefront modulation and subwavelength diffractive acoustics with an acoustic metasurface, Nat. Commun. **5**, 5553 (2014).

[14] Y. F. Zhu, X. Y. Zou, R. Q. Li, X. Jiang, J. Tu, B. Liang, and J. C. Cheng, Dispersionless manipulation of reflected acoustic wavefront by subwavelength corrugated surface, Sci. Rep. **5**, 10966 (2015).

[15] Z. L. Hou, X. Fang, Y. Li, and B. Assouar, Highly Efficient Acoustic Metagrating with Strongly Coupled Surface Grooves, Phys. Rev. Appl. **12**, 034021 (2019).

[16] Y. Zhu, X. Fan, B. Liang, J. Cheng, and Y. Jing, Ultrathin Acoustic Metasurface-Based Schroeder Diffuser, Phys. Rev. X **7**, 021034 (2017).

[17] Z. Li, H. Cheng, Z. Liu, S. Chen, and J. Tian, Plasmonic airy beam generation by both phase and amplitude modulation with metasurfaces, Adv. Opt. Mater. **4**, 1230 (2016).

[18] J. Zhao, B. Li, Z. Chen, and C. W. Qiu, Manipulating acoustic wavefront by inhomogeneous impedance and steerable extraordinary reflection, Sci. Rep. **3**, 2537 (2013).

[19] K. Melde, A. G. Mark, T. Qiu, and P. Fisher, Holograms for acoustics, Nature **537**, 518 (2016).

[20] Y. Xie, C. Shen, W. Wang, J. Li, D. Suo, B. I. Popa, Y. Jing, and S. A. Cummer, Acoustic holographic rendering with two-dimensional metamaterial-based passive phased array, Sci. Rep. **6**, 35437 (2016).

[21] Y. Tian, W. Qi, Y. Cheng, and X. Liu, Acoustic holography based on composite metasurface with decoupled modulation of phase and amplitude, Appl. Phys. Lett. **110**, 191901 (2017).

[22] Y. Zhu, J. Hu, X. Fan, J. Yang, B. Liang, X. Zhu, and J. Cheng, Fine manipulation of sound via lossy metamaterials with independent and arbitrary reflection amplitude and phase, Nat. Commun. **9**, 1632 (2018).

[23] Y. Zhu and B. Assouar, Systematic design of multiplexed-acoustic-metasurface hologram with simultaneous

amplitude and phase modulations, Phys. Rev. Mater. **3**, 045201 (2019).

[24] L. Zhang, R. Y. Wu, G. D. Bai, H. T. Wu, Q. Ma, X. Q Chen, and T. J. Cui, Transmission-reflection-integrated multifunctional coding metasurface for full-space controls of electromagnetic waves, Adv. Funct. Mater. **28**, 1802205 (2018).

[25] T. Cai, G. M. Wang, S. W. Tang, H. X. Xu, J. W. Duan, H. J. Guo, F. X. Guan, S. L. Sun, Q. He, and L. Zhou, High-Efficiency and Full-Space Manipulation of Electromagnetic Wave Fronts with Metasurfaces, Phys. Rev. Appl. **8**, 034033 (2017).

[26] K. J. B. Lee, M. K. Jung, and S. H. Lee, Highly tunable acoustic metamaterials based on a resonant tubular array, Phys. Rev. B **86**, 184302 (2012).

[27] E. Walker, D. Reyes, M. M. Rojas, A. Krokhin, Z. Wang, and A. Neogi, Tunable ultrasonic phononic crystal controlled by infrared radiation, Appl. Phys. Lett. **105**, 143503 (2014).

[28] Z. W. Wang, Q. Zhang, K. Zhang, and G. K. Hu, Tunable digital metamaterial for broadband vibration isolation at low frequency, Adv. Mater. **28**, 9857 (2016).

[29] Z. Tian, C. Shen, J. Li, E. Reit, Y. Gu, H. Fu, S. A. Cummer, and T. J. Huang, Programmable acoustic metasurfaces, Adv. Funct. Mater. 1808489 (2019).

[30] S. Zhai, K. Song, C. Ding, Y. Wang, Y. Dong, and X. Zhao, Tunable acoustic metasurface with high-Q spectrum splitting, Materials **11**, 1976 (2018).

[31] S. D. Zhao, A. L. Chen, Y. S. Wang, and C. Zhang, Continuously Tunable Acoustic Metasurface for Transmitted Wavefront Modulation, Phys. Rev. Appl. **10**, 054066 (2018).

[32] S. W. Fan, S. D. Zhao, A. L. Chen, Y. F. Wang, B. Assouar, and Y. S. Wang, Tunable Broadband Reflective Acoustic Metasurface, Phys. Rev. Appl. **11**, 044038 (2019).

[33] X. Jiang, Y. Li, and L. Zhang, Thermoviscous effects on sound transmission through a metasurface of hybrid resonances, J. Acoust. Soc. Am. **141**, EL363 (2017).

[34] E. G. Williams and J. A. Mann, Fourier acoustics. Sound radiation and nearfield acoustical holography, J. Acoust. Soc. Am. **108**, 1373 (2000).

[35] D. L. Liu and R. C. Waag, Propagation and backpropagation for ultrasonic wavefront design, IEEE Trans. Ultrason. Ferroelectr. Freq. Control **44**, 1 (1997).